Shape memory alloy (SMA)-cable-controlled sliding bearings: development, testing, and system behavior

Dong Liang [1,2], Yue Zheng [2], Cheng Fang [1,2,3*], Michael C H Yam [3], Chuntao Zhang[1]

[1] *Shock and Vibration of Engineering Materials and Structures Key Laboratory of Sichuan Province, Mianyang 621999, China*

[2] *College of Civil Engineering, Tongji University, Shanghai 200092, China*

[3] *Chinese National Engineering Research Centre for Steel Construction (Hong Kong Branch), The Hong Kong Polytechnic University, Hong Kong, China*

* *Corresponding author: email: chengfang@tongji.edu.cn, Tel: +86-(0)21-65982926*

Abstract: This paper presents an innovative type of friction sliding bearing system incorporating shape memory alloy (SMA) cables. The study commences with cyclic tests on individual SMA cables to understand their fundamental mechanical properties. The working principle of the proposed SMA-cable-controlled friction sliding bearing (SMA-sliding bearing) is subsequently described, followed by physical tests on two SMA-sliding bearing specimens. The bearing specimens show rectangular hysteresis loops induced by Coulomb friction before the SMA cables are stretched, and afterward the load resistance and energy dissipation capacity of the bearings are increased accompanied by certain self-centering capability due to the engagement of the SMA cables. Such action is expected to effectively restrict excessive displacements of the bearings and to help reduce the residual displacement. Following the experimental study, a theoretical model of the new bearing is developed and numerical simulation is carried out. The theoretical and numerical results agree very well with the experimental results. A case study focusing on a three-span continuous bridge subjected to pulse-like near-fault (NF) ground motions is subsequently conducted, where three types of bearing system, namely, conventional sliding bearing system, SMA-sliding bearing system, and steel-cable-controlled (steel-sliding) bearing system are compared. The system-level analysis results show that the proposed SMA-sliding bearing has its superiority in superstructure displacement control, with a limited increase in the curvature ductility of the pier.

Keywords: seismic resilience; shape memory alloy (SMA) cable; friction sliding bearing; bridge; experimental study; system-level analysis.

1. Introduction

Extreme events such as earthquakes can lead to severe damages or overturning of bridge structures, and as a result jeopardize the transportation network and compromise the effectiveness of post-hazard recovery. A field investigation organized by Han et al. [1] examined around 320 major bridges after the 2008 Wenchuan (China) earthquake. Among the damaged bridges, 14% were severely damaged, and 39% were moderately damaged. In particular, the damage was mainly associated with fallen girders and damaged bearings, in addition to failed bridge piers. The short-term and long-term impacts from the repair or replacement work for such damaged bridges accounted for the bulk of the total economic loss. Over the past decades, isolation bearings have been applied extensively in the construction of highway bridges and proved to be an effective solution for earthquake hazard mitigation. Friction sliding bearings are widely used in long span railway and highway bridges because of their large vertical load carrying and horizontal displacement capacities [2]. In addition, sliding isolation bearings are insensitive to the frequency range of the ground motion excitation compared with narrowed effective frequency ranges for rubber bearings [3]. Several reviews have been conducted on the historical development of the isolation bearing [4-5].

The essential idea of isolation bearings is to create a flexible interface that decouples the motions of superstructures and substructures. However, allowing increased flexibility is often accompanied by a weakening of the ability to control the displacement due to a lack of effective restraining mechanism. If the displacement of the girder exceeds the effective supporting range of the bearing or abutment, severe damage and even collapse could happen [6-7]. For example, many cases of unseating due to uncontrolled movement of the girder were reported after the 1989 Loma Prieta earthquake and 1994 Northridge earthquake [8-9]. In the 1995 Kobe earthquake, more than 60% of the severely damaged or collapsed bridges were found to experience unseating and collision/pounding due to large displacement [10]. In addition, more significant damages are induced in structures under near-fault (NF) earthquakes due to the high energy input [11-12]. It has been recognized that NF ground motions have special characteristics, such as rich long-period spectral components, large-amplitude velocity pulses and large peak ground acceleration (PGA) and velocity (PGV), compared with far-field records. Therefore, special attention should be paid to the control of bridge girder displacements under pulse-like NF ground motions.

To address the above issue, the concept of restrainers was proposed and confirmed to be effective in limiting large girder displacements [8, 13]. However, conventional bridge restrainers have certain limitations. For example, they are often demanding in installation and space, and many types of restrainers mainly play their role along the axial direction, i.e., they cannot provide sufficient load resistance in a direction perpendicular to their preset [14-16]. This disadvantage is more obvious in curved bridges due to the irregular configuration [17]. In addition, most restrainers such as steel and FRP ones are designed to work in their elastic range and therefore lack damping and buffering capabilities and have limited ductility [18]. A hybrid control system combining bearings with dampers was also developed and found to be effective [19], but this solution is quite complicated and costly. Dezfuli et al. [20-21] developed an SMA-wire-based rubber bearing, which utilized SMA wires as supplemental components to enhance the damping and displacement control capabilities, but some practical problems such as low resistance, stress concentration and effective gripping are yet to be resolved. Therefore, a more reliable and efficient approach to limit the bearing displacement during large earthquakes is still in need.

Shape memory alloy (SMA) possesses an intrinsic property of remembering its original shape [22]. The shape memory effect (SME) and the superelasticity (SE) are two well-known characteristics of SMA. The former allows the deformed material to regain its undeformed shape by heating, and the latter promotes spontaneous shape recovery upon unloading at room temperature. The reversible martensitic phase transformation is the essential reason behind the extraordinary behavior of the SMA [23]. In particular, superelastic SMAs provide a variety of advantages such as spontaneous self-centering capacity, stable energy dissipation ability and free of energy/power input, which makes them ideal candidates for passive seismic control.

In practice, superelastic SMAs are often made into various forms of components such as SMA bars, wires, cables, ring springs, coil springs, Belleville washers, and bolts [24-31]. As a relatively new family member of SMA elements, SMA cables reasonably hold many of the advantageous properties of conventional cables and exhibit extra benefits such as large recoverable deformation, energy dissipation capacity and excellent corrosion resistance [32]. In addition, SMA cables are highly ductile, reliable, and robust. They typically fail in successive rupture of the wires, so the failure process is not radical and less sensitive to initial imperfections. SMA cables have already been considered for seismic applications of bridges such as damping devices [33-36], in-span hinges [37] and restrainers [18, 38]. While their effectiveness in seismic mitigation has been confirmed by many numerical studies [18, 33-35, 38], test evidence is still very limited.

In this study, a friction sliding bearing combined with SMA cables is developed to improve the seismic performance of bridges. The cyclic behavior of individual SMA cables is experimentally studied first, and a proof-of-concept test on the proposed SMA-cable-controlled sliding bearings (SMA-sliding bearings) is subsequently carried out. The basic working mechanism of the novel system is described in detail, and its potential advantages over the conventional solutions are discussed. Finally, a case study of a three-span continuous beam bridge system is conducted to further investigate the effectiveness of the proposed SMA-sliding bearing. Preliminary design recommendations are also given based on the experimental and numerical results.

2. Cyclic behavior of individual SMA cables

2.1. Material

There are many classes of SMAs, among which the NiTi-based one (also known as Nitinol) is perhaps the most popular class in practical application. The chemical composition of the SMA wires used in this study is 50.8at.% nickel and 49.2at.% titanium alloys, and the material is expected to exhibit SE at room temperature. The monofilament wires are then used to produce the SMA cables.

The typical stress-strain curve of the SMA monofilament wire is illustrated in Fig. 1, where the ends of the SMA wire were clamped by flat wedge grips during the tests. A typical flag-shaped response with satisfactory recoverability can be seen. When the material is loaded, a transformation-induced plateau is exhibited when the stress exceeds the austenite-martensite transformation start stress

σ_{Ms}. The stress-induced transformation is completed at the austenite-martensite transformation finish stress σ_{Mf}. During unloading, a reverse phase transformation is triggered. By displaying a typical flag-shaped hysteresis, the material experiences the martensite-austenite transformation start stress σ_{As} and finish stress σ_{Af} successively, and finally returns to the original point with limited residual strain. A certain accumulation of residual strain accompanied by downward movement of the transformation plateau can be observed.

2.2. Cable specimens and test setup

As shown in Fig. 2, SMA cables with 7×7×1.2 and 12×12×1.0 layups/constructions were considered, where "7×7×1.2" means that each cable is composed of seven strands and each strand has 7 wires with 1.2 mm diameter. The same terminology is used for "12×12×1.0" cables. The total length (including the gipped region) of each cable specimen was approximately 284 mm and the effective length of the free segment, i.e., the length between the inner edges of the two end holding bars, was 164 mm. The detailed dimensions of the SMA cable specimens are given in Fig. 2. The ends of the cables were melt-cut and firmly embedded into the end holding bars to prevent unraveling. The end holding bars were threaded for convenient installation in practical application.

An MTS universal test machine with a load capacity of 250 kN was employed to apply the uniaxial load on the SMA cable specimens, as shown in Fig. 2. The top and bottom hydraulic wedge grips tightly clamped the two ends of the cable. Two cyclic loading protocols, namely, load with incremental amplitudes and load with constant amplitude, were considered. For the former, the global strain ε_o was increased from 1% to 10% with a 1% interval and each strain level was repeated twice. For the latter case, a constant global strain amplitude of 6% was repeated for 20 cycles. Three cables were tested, with the test code and details given in Table 1. The average stress of the SMA cable can be obtained by dividing the cable force by the sectional area, i.e. the sum of the area of all the monofilament wires. The global strain ε_o was determined by $\varepsilon_o = \Delta L/L_f$, where ΔL = axial elongation recorded by the MTS, and L_f = length of free segment of the SMA cable (i.e., 164 mm).

2.3. Test results and discussion

2.3.1. Strength and stiffness

Fig. 3(a) shows the stress-strain curves of cable specimens 7×7×1.2-I and 12×12×1.0-I. The peak stress increases with increasing cycles, which is accompanied by stress degradation caused by cable relaxation and functional fatigue (transformation-induced fatigue, TIF) of SMA [32, 39-40]. The former factor also exists in conventional cables, whereas the latter is a unique behavior of SMA. The exact "contribution" from the two factors is difficult to ascertain, but appropriate "pre-training" can reduce the degradation effect and stabilize the hysteresis. It is also obvious that there are some differences in the hysteretic shapes of the two cable specimens. In particular, 12×12×1.0-I exhibits a lower initial stiffness than that of 7×7×1.2-I, which is probably attributed to the different construction/layup details (noting that 12×12×1.0 is not a standard cable layup) and different batches of SMA wires. The observation implies that the process of production can have an influence on the mechanical property of the SMA cables. In fact, existing studies showed that the behavior of SMA cables is sensitive to layup details and also the behavior of the monofilament wires [32, 39-40]. For the case of constant amplitudes (Fig. 3(b)), i.e., 7×7×1.2-C, the peak stress was constant and the flag-shaped hysteresis becomes stabilized after a few loading cycles. These indicate that the degradation phenomenon does not affect the peak load, although the "yield" load and energy dissipation could be affected. This property is essential for seismic application of the SMA cables (e.g., restrainers for bridges) because a reliable and sufficient load-carrying capacity at relatively large deformations is desired. The change of the yield strength of the SMA cable specimens is shown in Fig. 4(a).

Fig. 4(b) shows the measured elastic moduli of the three cable specimens. Similar to the yield strength, the elastic modulus of specimen 7×7×1.2-C under constant cyclic load tends to stabilize with increasing cycles. For the specimens under incremental cyclic load, the elastic modulus decreases with loading cycles due to the degradation effect. Due to the different constructions, the elastic modulus of 12×12×1.0-I is consistently lower than that of 7×7×1.2-I.

2.3.2. Self-centering capability

As shown in Fig. 4(c), different accumulations of residual strain are shown in the specimens. For those under incremental cyclic loading, the residual strain continues to increase with increasing peak strains. The total residual strain for specimen 7×7×1.2-I is close to 1.2%, corresponding to a recoverable rate, i.e., the proportion of the restored strain to the achieved maximum strain, of 88%. The total residual strain of 12×12×1.0-I is nearly 1.5% which is higher than that of 7×7×1.2-I. On the contrary, the specimen under constant cyclic loading develops the largest residual strain during the initial loading cycle, and then the increase in residual strain slows down. Specifically, the accumulated residual strain of 7×7×1.2-C within the first eight cycles accounts for more than 80% of the final residual strain (20 cycles). This again confirms that an appropriate “pre-training” is necessary for reducing the residual strain during the service life of SMA cables.

2.3.3. Energy dissipation

Apart from the expected self-centering capability, SMA cables are supposed to display appropriate energy dissipation capacity. A dimensionless index, namely, equivalent viscous damping (EVD), is often employed as an indicator of energy dissipation capacity, as expressed by:

$$EVD = \frac{W_D}{4\pi W_E} \tag{1}$$

where W_D = energy loss within a closed hysteretic loop. i.e., the total area of a given cycle; W_E = elastic energy accumulated along a linear stress-strain response with the same maximum value of displacement as that of the nonlinear system. As shown in Fig. 4(d), the EVD of the specimen under constant loading (7×7×1.2-C) is up to 3.8%, and the value decreases most significantly during the first few cycles and then becomes stabilized. The EVD of the specimens under incremental cyclic loading (7×7×1.2-I and 12×12×1.0-I) increases more obviously in the first few loading cycles. At large strain, a slight decrease in EVD is seen, which is due to an obvious rising of the peak point of the hysteretic loop but no significant change in the loop area W_D (see Eq. (1)).

3. Proposed SMA-cable-controlled sliding bearing

3.1. Statement of problem and working principle of proposed bearing

A novel sliding bearing equipped with SMA cables is proposed herein. The SMA cables are expected to restrain the bearing when excessive displacement occurs, and in addition, to provide supplemental damping and self-centering capability at large displacements. In this study, a conventional friction sliding bearing system is considered as the basic element. A conventional friction sliding bearing acts by sustaining shear force through the generated Coulomb friction from the sliding interface, hence friction is the main source of energy dissipation for conventional sliding bearings. Problems such as excessive and unconstrained displacement in the friction sliding bearings have been criticized, despite the advantages such as insensitivity to the range of excitation frequency [3]. There is solid evidence that extremely large bearing displacement would cause a collision of adjacent components and failure of side blocks and center curb [41-42]. Besides, the high energy shockwave caused by pounding may result in severe and irreversible damage to other main components of the bridge, e.g., the pier [43]. An isolator equipped with a phased/gap damper was developed and numerically analyzed [44]. When the relative displacement is larger than the intended gap, the damper starts to act. The analytical result indicates that the gap damper can effectively decrease the displacement of the isolator. Some inspirations can be acquired from this concept.

Fig. 5 gives a schematic illustration of the bearing and a three-dimensional view of its main parts. The friction sliding bearing consists of a top plate, stainless steel plate, PTFE plate, steel plate, rubber pad, and bottom plate. These are the main components for sustaining the vertical load and providing horizontal displacement. The SMA cables are considered as the key supplemental elements for restraining purposes. These cables are connected to the top and bottom plates through spherical hinges (Fig. 5(b)) which are accommodated by the pre-opened holes of these plates. Grease is applied to the holes to facilitate free rotation so that the cables are mainly subjected to tensile force (within a predetermined range). When applied in practice, some parameters, such as geometric details of the spherical hinges and holes, frictional coefficient of the sliding surface and the number and size of the SMA cables, should be adjusted as needed.

Fig. 6 further illustrates the behavior of the bearing along with the horizontal load-displacement responses of the different elements at varying stages. The SMA-sliding bearing first exhibits a load-displacement response similar to conventional sliding bearing before reaching the initial gap (Fig. 6(a)).

This stage allows the free movement of the bearing caused by shrinkage, creep or temperature change. The initial gap in one direction (l_{gap}) can be expressed by:

$$l_{gap} = \sqrt{{l_{eff}}^{2} - h^{2}} \tag{2}$$

In the equation, h is the vertical distance between the rotation center of the top and bottom spherical hinges; l_{eff} is the effective length of the SMA cable between the rotation center of the two spherical hinges. The value of l_{gap} can be adjusted according to practical needs. As the behavior of the bearing at this stage depends on the friction, the lateral resisting force $F_{SMA\text{-}sliding}$ can be expressed by:

$$F_{SMA-sliding} = \mu W_{G} \tag{3}$$

where W_G is the vertical load applied to the bearing; μ is the frictional coefficient of the sliding surface of the bearing.

When the relative displacement exceeds the initial gap, the SMA cables are mobilized and start to provide supplemental damping (Fig. 6(b)). A single-degree-of-freedom model with two “springs” (one for friction and the other one for the horizontal component of the force provided by the SMA cables) can well capture the basic characteristics of the bearing. In this stage, the total lateral resisting force of the bearing $F_{SMA\text{-}sliding}$ can be expressed by:

$$F_{SMA-sliding} = \mu(W_{G} + F_{SMA\text{-}V}) + F_{SMA\text{-}H} \tag{4}$$

where $F_{SMA\text{-}H}$ and $F_{SMA\text{-}V}$ is the horizontal and vertical components of the force provided by the SMA cables, respectively. According to the geometric relationship (Fig.6 (b)), $F_{SMA\text{-}H}$ and $F_{SMA\text{-}V}$ can be calculated by:

$$F_{SMA\text{-}H} = \sigma_{SMA} A_{sum} \sin\theta \tag{5}$$

$$F_{SMA\text{-}V} = \sigma_{SMA} A_{sum} \cos\theta \tag{6}$$

where σ_{SMA} is the stress of the SMA cables; A_{sum} is the total cross-sectional area of all the SMA cables used in the bearing; θ is the angle between the SMA cable and the vertical axis, as expressed by:

$$\sin\theta = \frac{\Delta l + l_{gap}}{\sqrt{(\Delta l + l_{gap})^2 + h^2}} \tag{7}$$

$$\cos\theta = \frac{h}{\sqrt{(\Delta l + l_{gap})^2 + h^2}} \tag{8}$$

where Δl is the further displacement of the bearing after the initial gap. A typical flag-shaped hysteretic model with a limited number of controlling parameters is often adequate for describing the basic behavior of superelastic SMA cables, as shown in Fig.7, in which case σ_{SMA} can be calculated by the following set of equations:

$$\varepsilon_{SMA} = \frac{\sqrt{(\Delta l + l_{gap})^2 - h^2} - l_{eff}}{l_{eff}} \tag{9}$$

1）loading

$$\sigma_{SMA} = \varepsilon_{SMA} E \qquad \text{for } \varepsilon_{Ms} > \varepsilon_{SMA} > 0 \tag{10}$$

$$\sigma_{SMA} = \sigma_{Ms} + (\varepsilon_{SMA} - \varepsilon_{Ms})\beta_1 E \qquad \text{for } \varepsilon_{Mf} > \varepsilon_{SMA} > \varepsilon_{Ms} \tag{11}$$

$$\sigma_{SMA} = \sigma_{Mf} + (\varepsilon_{SMA} - \varepsilon_{Mf})\beta_2 E \qquad \text{for } \varepsilon_{SMA} > \varepsilon_{Mf} \tag{12}$$

2) unloading

$$\sigma_{SMA} = \sigma_{Mf} + (\varepsilon_{SMA} - \varepsilon_{Mf})\beta_2 E \qquad \text{for } \varepsilon_{SMA} > \varepsilon_{Mf} \tag{13}$$

$$\sigma_{SMA} = \sigma_{Mf} - (\varepsilon_{Mf} - \varepsilon_{SMA}) E \qquad \text{for } \varepsilon_{Mf} > \varepsilon_{SMA} > \varepsilon_{As} \tag{14}$$

$$\sigma_{SMA} = \sigma_{As} - (\varepsilon_{As} - \varepsilon_{SMA})\beta_1 E \qquad \text{for } \varepsilon_{As} > \varepsilon_{SMA} > \varepsilon_{Af} \tag{15}$$

$$\sigma_{SMA} = \varepsilon_{SMA} E \qquad \text{for } \varepsilon_{Af} > \varepsilon_{SMA} > 0 \tag{16}$$

where ε_{SMA} is the strain of the SMA cables, and the other symbols are explained in Fig. 7.

The proposed bearing may have the following extra benefits compared with some existing

SMA wire-based or cable-based bearing solutions [20-21, 42, 45-48]: 1) all the SMA cables can work simultaneously when the bearing plate moves in any horizontal direction, i.e., 360-degree effective; 2) the SMA cables can also control excessive vertical displacements of the bearing under vertical seismic excitations; and 3) the connections between the SMA cables and bearing plates are flexible so that no stress concentration occurs in the cables within the design displacement. It is noted that direction-changing steel hooks [20-21] or U-shape cable configuration [42, 45-48] in the existing solutions could cause premature failure of the SMA wires/cables.

3.2. Bearing specimen and test arrangement

Quasi-static tests on a proof-of-concept bearing specimen were conducted. The geometric configuration and the detailed dimensions of the specimen are shown in Fig. 8(a). Two tests were conducted successively on the same bearing specimen with different numbers of SMA cables. The repeated use of the friction sliding bearing is acceptable as there is no damage to the bearing and the properties of the sliding friction surface are not significantly changed by repeated experiments. In the two tests, namely, tests 2-SC and 4-SC, 2 and 4 new SMA 12×12×1.0 cables were employed, respectively, although more cables can be used in practice if necessary. The cables were placed symmetrically on the two sides of the bearing. The material, detailed manufacturing procedure, and configuration were the same as the 12×12×1.0 SMA cables described in section 2.1. The end gripping technique for the SMA cable was the same as that used for the individual cable described in Section 2, where both ends were merged into the threaded holding bars to facilitate assembly with the spherical hinges that have matching threads. The pre-opened holes in the top and bottom plates provide an available free rotation of 30 degrees (Fig. 8(b)), corresponding to a horizontal displacement of around

95 mm. Local bending action would be induced to the cables once this displacement is exceeded. Larger free rotation can be achieved by changing the dimension/shape of the pre-openings.

The test setup for the bearing specimen is schematically shown in Fig. 8(c). The bearing was placed horizontally between the top and bottom loading plates. The vertical load and the lateral load were applied to the top and bottom plates, respectively, by two electro-hydraulic servo actuators. A vertical load of 3000 kN was applied for the current specimen. The displacement amplitude started from 40 mm to 95 mm (maximum design displacement) with an incremental interval of 5 mm for both tests. Two identical loading cycles were performed at the same amplitude. A linear variable differential transformer (LVDT) was placed at the edge of the bottom loading plate (Fig. 8(c)) to record the horizontal displacement of the bearing plate.

3.3. Test results and discussions

The typical deformation modes of the bearing specimen are presented in Fig. 9. As anticipated, the SMA cables were relaxed at the beginning and then started to contribute to load resistance after the initial gap. The spherical hinges rotated as expected, and hence the bending action of the cable was insignificant prior to the rotation limit. At the maximum considered displacement of 95 mm, the inclination angle of the SMA cables was approximately 30 degrees as intended, and the SMA cables were generally intact. Although a few wires were found to fracture or slip out of the grippers/holding bars, this local "failure" basically had no significant influence on the overall function of the SMA cables during the test. Fig. 10 gives the horizontal load-displacement response for the two tests. Rectangular hysteresis caused by friction only is observed before the initial gap. The constant load (F_0) is around ±15 kN in both tests, so the friction coefficient can be estimated as follows:

$$\mu = \frac{F_0}{P} \tag{17}$$

where P is the applied vertical load = 3000 kN, and therefore the friction coefficient is approximately 0.005. When the lateral displacement reaches the initial gap, the load resistance increases dramatically as the SMA cables began to engage. Increased energy dissipation is also observed which was contributed by both frictional and superelastic effect. In addition, an obvious self-centering tendency of the bearing can be observed beyond the initial gap, and the entire hysteretic loops are quite stable.

Large residual displacement still exists due to the friction, but it is noted that the actual residual displacement under "dynamic shakedown" is expected to be smaller than the value from static unloading [49]. The self-centering tendency provided by the SMA cables is expected to decrease the residual displacement under dynamic excitations, as discussed later in the system-level analysis.

The hysteretic responses from the two tests are further compared in Fig. 11(a). As anticipated, the load resistance of specimen 4-SC is nearly twice as large as that of specimen 2-SC at the same displacement. The energy dissipation per cycle is calculated and illustrated in Fig. 11(b). The energy dissipation contributed by friction can be estimated roughly by a straight line passing through the data before the initial gap. As observed in the figure, the energy dissipation deviates from the straight line beyond the initial gap, indicating extra energy dissipation contributed by the SMA cables. It can be deduced from the figure that the SMA cables are responsible for 30% of the total energy dissipation at the last cycle. In practice, the load-carrying capacity of such bearings is tunable, therefore limiting the displacement under the maximum considered earthquake (MCE) can be achieved by appropriately designing the SMA cables.

4. Case study

4.1. Bridge description

To demonstrate the effectiveness of the proposed bearing, a typical three-span continuous reinforced concrete (RC) box-girder bridge is selected as an example for investigation. The conventional and new SMA-sliding bearings are considered for this bridge; however, to expand the discussion, steel-cable-controlled sliding (steel-sliding) bearings are further considered. The resulting seismic performances from the three cases are compared. The geometric layout and details of the bridge is shown in Fig. 12(a), where the side and middle spans are 20m and 30m, respectively. The design compressive strength of the concrete used in the girder and pier is 40.0 MPa. The yield strengths (f_y) of the longitudinal and transversal reinforcements are 440.0 MPa and 280.0 MPa, respectively. A total of 20 longitudinal reinforcing rebars are uniformly arranged along the circumference of the column, resulting in a reinforcement ratio of 1.94%. The distance between two adjacent stirrups is 0.125 m, and the corresponding reinforcement ratio is 0.2%. The thickness of the concrete cover of the pier is 0.065 m. The Young's moduli of the reinforcement and concrete are assumed to be 2.0×10^5 MPa and 3.0×10^4 MPa, respectively. It is assumed that the required separation distance between the bridge deck and the abutment is provided [50-52]. The friction coefficient of the sliding bearings in both the conventional and novel bridges is 0.06, according to CLATRANS [53]. The SMA cables which are initially slack are capable of providing a 0.1 m free movement for the bearing. The total necessary cross-sectional area of the SMA cables can be determined based on the following design criteria (Fig. 12(b)): (1) the strain of the SMA cables remains at the elastic range under the frequently-occurring earthquake (FOE); (2) the strain of the SMA cables does not exceed the fully-recoverable strain, which is typically 10%, under the design-based earthquake (DBE); (3) the strain of SMA cables does not advance into the plastic strain range under the maximum considered earthquake (MCE); (4) the SMA cables do not fracture after experiencing an earthquake beyond the MCE (fracture strain is typically 20~25%). To quantify the SMA cable design, a specific indicator α is proposed, i.e., the ratio of the total horizontal force ($F_{SMA\text{-}H}$) provided by the SMA cables at 10% strain (the fully-recoverable strain) to the inertia force of the girder ($F_{inertia}$).

$$F_{SMA-H} = \alpha F_{inertia} = \alpha m_g Sa(\mathrm{T}, \xi) \tag{18}$$

In the equation, m_g denotes the mass of the girder, and T is the natural period determined by modal analysis. The damping ratio (ξ) of the bridge is assumed to be 5%, and the spectral acceleration $Sa(T, \xi)$ of the bridge can be obtained. With a given value of α, the required area of the SMA cables can be calculated from Eqs. (5) and (14). Based on a preliminary analysis, α is temporarily assumed to be 0.50 to ensure that the maximum cable strain is generally within 10% under the design earthquake. The resulting total cross-sectional area of the SMA cables for each bearing is 2148 mm^2, corresponding to 19 12×12×1.0 cables. For comparison purpose, the same area of steel cables is used.

4.2. Modeling strategy and validation

A 3D finite element (FE) model of the bridge was established in OpenSees [54], as shown in Fig. 13. Elastic beam-column elements were utilized to model the RC box-girder decks and pier caps since they typically remain elastic even under strong ground motions. The total mass of the bridge deck is 9.36×10^5 kg. Displacement-based nonlinear fiber elements were used to model the piers. The behavior of the reinforcement was represented by a uniaxial Menegotto-Pinto constitutive model. The uniaxial Kent-Scott-Park concrete model was used to simulate the unconfined and confined concretes. The soil-structure interaction (SSI) of each foundation was modeled by six zero-length spring elements

[53]. The present study mainly focuses on the bridge response in the longitudinal direction, which is a governing scenario [55]. In the meantime, the shear keys, which are usually utilized for controlling the transverse vibration of the bridge, are not considered here [50-52].

As explained in Fig. 13, the SMA-sliding bearing was simulated by combining an elastic perfectly plastic element and two impact elements in parallel. The former represents the friction behavior of the bearing, and the latter is used to consider the restraining effect of the SMA cables. With the stress-strain relationship (i.e., Table 2 and Fig. 7) and length of the SMA cables known, the theoretical behavior of the SMA-sliding bearing can be obtained considering the evolving geometric relationships as expressed in Eqs. (2) through (16). The resulting theoretical predictions are compared with the two test results, as shown in Fig. 14. The obtained response is then directly simulated by the numerical model. The impact element in OpenSees with variable stiffness could well describe the fundamental behavior of the SMA-sliding bearing, as confirmed in Fig. 14.

The validated modeling strategy was utilized for the case study. Except for l_{eff} which is adjusted to 242 mm, the basic SMA cable parameters given in Table 2 were used. The key input parameters in OpenSees for the bearing behavior are summarized in Table 3, where the symbols have been explained in Fig. 13. A similar simulation approach was used for modeling the steel-sliding bearing (Fig. 13). Standard steel cables with a yield strain of ε_y=1.75% (corresponding to yield stress $f_{y,\mathrm{steel}}$ = 1210 MPa) and elastic modulus of E_{steel} = 69 GPa were considered [18, 45, 56].

4.3. Selected ground motions

As bridge systems are more susceptible to NF ground motions which exhibit large-amplitude velocity pulses, a suite of 7 NF earthquake records collected from the Pacific Earthquake Engineering

Research (PEER) strong motion database [57] were selected for the seismic analysis, as summarized in Table 4 and shown in Fig. 15. The design response spectrum was constructed based on a soft rock site in southwest California [58]. It is worth mentioning that unlike far-field (FF) ground motions which are uniformly scalable, the pulse period of NF ground motions is highly related to the source properties such as the rise time and rupture dimensions. As a result, a uniform scaling process could violate the critical pulsing characteristics [59]. In light of this, the selected NF ground motion records were not scaled in order to reflect the "true" pulsing properties. As observed in Fig.15, the mean acceleration response spectrum of the selected NF ground motions is not less than the target spectrum (DBE level).

4.4. Discussion of analysis results

The relative displacement of the bearing, curvature ductility of the RC pier and residual displacement of the girder were considered as the main performance indices for damage assessment of the bridge. Curvature ductility is defined as the maximum curvature divided by the yield curvature. Fig. 16 shows the monotonic moment-curvature response of the RC pier, from which the equivalent yield curvature and its corresponding bending moment can be obtained. An impact percentage factor (IPF) [34] is proposed for providing a clearer comparison between the conventional and restrained bridge systems, as expressed by:

$$IPF = \frac{E_{\mathrm{C}} - E_{new}}{E_{\mathrm{C}}} \times 100\% \tag{19}$$

where E_C and E_{new} are the results of interest of the bridges with conventional and new SMA-sliding/steel-sliding bearing systems, respectively. A positive value of IPF means that the new system decreases the seismic response. On the contrary, a negative value suggests that the introduction of the new system increases the performance indicator.

The key system analysis results are summarized in Tables 5 through 7. In general, the proposed SMA-sliding and steel-sliding bearing systems effectively suppress the peak and residual displacements of the bearings. The typical force-displacement responses of the conventional, SMA-sliding and steel-sliding bearings under the Tabas and Landers earthquakes are presented in Fig. 17. For the conventional bearing, the load resistance provided by the friction force is constant and the displacement is quite large. Both supplemental SMA and steel cables could limit the bearing displacement with similar effectiveness. However, the steel cables have a maximum peak strain of 8.1%, which means that they experience severe plastic deformation. This might lead to failure of the restrainers and the associated connectors during extreme events, and the damaged steel cables have to be replaced after the earthquake, which compromises the process of post-earthquake recovery. On the other hand, the maximum and average peak strains of the SMA cables are 10.9% and 6.3%, respectively, which is generally within the fully recoverable strain range. Another potential benefit of the SMA cables is their excellent corrosion resistance, which makes them more attractive when employed under chloride environment.

The decrease in the bearing displacement responses is at the cost of increase in the curvature ductility of the pier to various degrees. The average pier curvature ductility of SMA-sliding bearing system is 1.01, corresponding to a 22.74% increase compared with the curvature ductility of the conventional pier. Nevertheless, the damage to the pier is still minor, noting that a curvature ductility of less than unity means no significant damage. As the initial stiffness and yield strength of the steel cables are much larger than those of the SMA counterpart, a more severe “shock” to the bridge substructure is anticipated when the cables are stretched. This is confirmed by Table 7, where the average increasing ratio of curvature ductility for the steel-sliding bearing system is 40.32%, which is nearly twice that of the SMA-sliding bearing system. It should be noted that the current practice actually does not allow yielding of the steel restrainers, so in practice more steel cables should be used rather than assuming the same cross-sectional area of the SMA cables in the present study. This would cause even more significant damage to the pier.

The typical time-history responses of the bearing displacement and curvature ductility of the pier are further shown in Fig. 18. The conventional bearing travels a large distance under pulse excitations but the SMA-sliding and steel-sliding bearings always move within a safe range. As a result of the large excursion, the residual displacement of the conventional sliding bearing is much larger than that of the improved bearings. The occurrence of the maximum ductility curvature generally echoes the time when the peak bearing displacement occurs. Again, using steel cables leads to increased maximum curvature ductility. It is worth mentioning that the reductions in peak and residual bearing displacement can be further “optimized” by tuning the initial gap (slack) or the amount of SMA cables. In addition, the sensitivity to the bearing details varies significantly with different bridge types. A more comprehensive parametric study may be carried out to achieve an optimal design of the SMA-sliding bearing, but this will be reserved for future studies.

5. Conclusions

This paper has shed considerable light on the application of SMA cables for the bearings in seismic resilient bridges. The fundamental mechanical behavior of individual SMA cables was first studied, followed by proof-of-concept tests on SMA-cable-controlled sliding bearing specimens. A case study on a three-span continuous bridge was then carried out to investigate the effectiveness of the proposed bearing system. In general, the feasibility of the novel SMA-cable-controlled sliding bearing system against seismic action is affirmed, and the following observations and conclusions are particularly noted:

- The individual SMA cable exhibited typical flag-shaped hysteretic curves with a recovery rate of more than 85% after experiencing a peak strain amplitude of 10%, accompanied by moderate energy dissipation capacity.
- The degradation of the SMA cables after undergoing several load cycles can be attributed to the TIF effect; however, a proper "pre-training" process could be effective in stabilizing the hysteretic response.
- The proposed bearing system was effectively restrained by the SMA cables which provided large load resistance, certain self-centering capability and additional damping at large displacements. The SMA cables are easy to examine and even replace when necessary after extreme events.
- The system analysis confirmed that the SMA-sliding bearing encourages enhanced displacement control capability with a minor increase in the pier curvature ductility. Such phenomenon could effectively prevent unseating of the superstructure during extreme events, especially under NF earthquakes. The reduction of the residual displacement also minimizes the bearing damage and accelerate the post-earthquake repair process.
- Replacing the SMA cables in the bearing with steel cables with the same total cross-sectional area leads to similar displacement control efficiency but increased damage to the pier. In addition, the steel cables experience significant damage and hence need to be replaced after the earthquake.

6. Acknowledgment

The financial support from the National Natural Science Foundation of China (NSFC) with Grant Nos. 51778456 and 51978513 is gratefully acknowledged. Support for this study is also provided by the Shock and Vibration of Engineering Materials and Structures Key Laboratory of Sichuan Province (18kfgk05) and the Chinese National Engineering Research Centre for Steel Construction (Hong Kong Branch).

7. References

[1] Han Q, Du X, Liu J, Li Z, Li L, Zhao J. Seismic damage of highway bridges during the 2008 Wenchuan earthquake, Earthquake Engineering and engineering vibration. 8,263-273, 2009.

[2] Dolce M, Cardone D, Palermo G. Seismic isolation of bridges using isolation systems based on flat sliding bearings. Bulletin of Earthquake Engineering, 5, 491-509, 2007.

[3] Kunde MC, Jangid RS, Effects of Pier and Deck Flexibility on the Seismic Response of Isolated Bridges, Journal of Bridge Engineering, 109, 1084-0702, 2006.

[4] Kelly JM. A seismic base isolation: a review and bibliography. Soil Dynamics and Earthquake Engineering, 5, 202-16, 1986.

[5] Ibrahim RA. Recent advances in nonlinear passive vibration isolators, Journal of Sound and Vibration 314, 371-452, 2008.

[6] Hsu YT, Fu C. Seismic effect on highway bridges in Chi Chi earthquake. Journal of Performance of Constructed Facilities, 18(1), 47-53, 2004.

[7] Ghobarah A, Ali HM. Seismic performance of highway bridges. Engineering Structures, 10(3),157-166,1988.

[8] Saiidi M, Maragakis E, Abdel-Ghaffar S, Feng, S, O’Connor D. Response of bridge hinge restrainers during earthquakes—field performance, analysis, and design. Ctr. for Civil Engineering. Earthquake Research. University of Nevada, Reno, Nev. Rep. No. CCEER 93/06, 1993.

[9] Moehle JP. Northridge earthquake of January 17, 1994: Reconnaissance report, Volume 1-Highway bridges and traffic management. Earthquake Spectra, 11(3), 287-372, 1995.

[10] Comartin C, Green M, Tubbesing S. The Hyogo-Ken Nanbu earthquake. Preliminary Reconnaissance Rep., Earthquake Engineering Research Institute, Oakland, California, 1995.

[11]Jangid RS , Kelly JM. Base isolation for near-fault motions, Earthquake Engineering Structure Dynamics, 30(5), 691-707, 2001.

[12] Bhasker Rao P, Jangid R S. Performance of sliding systems under near-fault motions, Nuclear Engineering, 203(2-3), 259-272, 2001.

[13] Priestley MJN, Seible F, Uang CM. The Northridge earthquake of January 17, 1994: Damage analysis of selected freeway bridges. Department of Applied Mechanics and Engineering Sciences, University of California, San Diego. Rep, No. SSRP-94/06, 1994.

[14] Shrestha B, Hao H, Bi K. Devices for protecting bridge superstructure from pounding and unseating damages: an overview. Structure and Infrastructure engineering, 13(3) 313-330, 2017.

[15] DesRoches R, Pfeifer T, T. Leon R, Lam T. Full-Scale Tests of Seismic Cable Restrainer Retrofits for Simply Supported Bridges. Journal of Bridge Engineering, 8(4), 191-198, 2003.

[16] DesRoches R, Delemont M. Seismic retrofit of simply supported bridges using shape memory alloys. Engineering Structures, 24, 325-332, 2002.

[17] Guo J, Zhong J, Dang X, Yuan W. Influence of Multidirectional Cable Restrainer on Seismic Fragility of a Curved Bridge. Journal of Bridge Engineering, 24(3), 04019001, 2019.

[18]Li S, Dezfuli F H, Wang J Q, Alam M S. Displacement-Based Seismic Design of Steel, FRP, and SMA Cable Restrainers for Isolated Simply Supported Bridges, Journal of Bridge Engineering, 23(6), 2018.

[19] Kawashima K, Unjoh S. Seismic response control of bridges by variable dampers. Journal of Structural Engineering, 120(9), 6909, 1994.

[20] Dezfuli FH, Alam MS. Shape memory alloy wire-based smart natural rubber bearing. Smart Materials and Structures, 22,045013 (17), 2013.

[21] Dezfuli FH, Alam MS. Hysteresis model of shape memory alloy wire-based laminated rubber bearing under compression and unidirectional shear loadings. Smart Materials and Structures, 24,065022 (19), 2015.

[22] Jani JM, Leary M, Subic A, Gibson MA. A review of shape memory alloy research, applications and opportunities. Materials and Design, 56, 1078-113, 2014.

[23] Fang C, Wei W, Shape memory alloys: modeling and engineering applications. Nature Singapore: Springer Nature Singapore, 2020.

[24] Zheng Y, Dong Y, Performance-based assessment of bridges with steel-SMA reinforced piers in a life-cycle context by numerical approach, Bulletin of Earthquake Engineering, 17(3), 1667-1688, 2019.

[25] Wang W, Fang C, Liu J. Large size superelastic SMA bars: heat treatment strategy, mechanical property and seismic application. Smart Materials and Structures, 25(7), 075001, 2016.

[26] Fang C, Yam MCH, Ma HW, Chung KF. Tests on superelastic Ni-Ti SMA bars under cyclic tension and direct-shear: towards practical recentring connections. Materials and Structures, 48(4), 1013-30, 2015.

[27] Qiu C, Zhu S. Shake table test and numerical study of self-centering steel frame with SMA braces. Earthquake Engineering and Structural Dynamic, 46, 117-137, 2017.

[28] Zheng Y, Dong Y, Li Y. Resilience and life-cycle performance of smart bridges with shape memory alloy (SMA)-cable-based bearings. Construction and Building Materials, 158, 389-400, 2018.

[29] Fang C, Yam MCH, Chan TM, Wang W, Yang X, Lin X. A study of hybrid self-centring connections equipped with shape memory alloy washers and bolts. Engineering Structures, 164, 155-168, 2018.

[30] Wang W, Fang C, Yang X, Chen YY, Ricles J, Sause R. Innovative use of a shape memory alloy ring spring system for self-centering connections. Engineering Structures, 153,503-15, 2017.

[31] Fang C, Zhou XY, Osofero AI, Shu Z, Corradi M. Superelastic SMA Belleville washers for seismic resisting applications: experimental study and modelling strategy. Smart Materials and Structures, 25, 105013, 2016.

[32] Reedlunn B, Daly S, Shaw J. Superelastic shape memory alloy cables: Part I– Isothermal tension experiments. International Journal of Solids and Structures. 50, 3009-3026, 2013.

[33] Zhang Y, Hu X, Zhu S. Seismic performance of benchmark base-isolated bridges with superelastic Cu-Al-Be restraining damping device. Structural Control and Health Monitoring, 16:668-685, 2009.

[34] Aryan H, Ghassemieh M. Seismic enhancement of multi-span continuous bridges subjected to three-directional excitations," Smart Material and Structure, 24(4), 2015.

[35] Aryan H, Ghassemieh M. A superelastic protective technique for mitigating the effects of vertical and horizontal seismic excitations on highway bridges, Journal of Intelligent Material System Structure, 28(12), 1533-1552, 2017.

[36] Liu A, Liu C, Fu J, Pi Y, Huang Y, Zhang J. A Method of Reinforcement and Vibration Reduction of Girder Bridges Using Shape Memory Alloy Cables. International Journal of Structural Stability and Dynamics, 17(7), 1750076, 2017.

[37] Johnson R, Padgett JE, Maragakis ME, DesRoches R , Saiidi MS. Large scale testing of nitinol shape memory alloy devices for retrofitting of bridges, Smart Material and Structure, 17035018(10pp), 2008.

[38] Li S, Dezfuli FH, Wang J, Alam MS. Performance-based seismic loss assessment of isolated simplysupported highway bridges retrofitted with different shape memory alloy cable restrainers in a life-cycle context. Journal of Intelligent Material Systems and Structures, 1-23, 2020.

[39] Fang C, Zheng Y, Chen J, Yam MC, Wang W. Superelastic NiTi SMA cables: Thermal-mechanical behavior, hysteretic modelling and seismic application, Engineering Structures, 183, 533-549, 2019.

[40] Sherif M M, Ozbulut O E. Tensile and superelastic fatigue characterization of NiTi shape memory cables, Smart Material. Structure, 27(1), 2018.

[41] Kawashima K, Takahashi Y, Ge H, Wu Z, Zhang J. Reconnaissance Report on Damage of Bridges in 2008 Wenchuan, China, Earthquake. Journal of Earthquake Engineering, 13,965-996, 2009.

[42] Wei Z, Yuan W, Cheung P, Cao X, Rong Z. Seismic Performance of Continuous Girder Bridges Using Cable-sliding Friction Aseismic Bearing. Procedia Engineering, 14,914-921, 2011.

[43] Guo A, Li Z, Li H, Ou J. Experimental and analytical study on pounding reduction of base-isolated highway bridges using MR dampers. Earthquake Engineering and Structural Dynamic, 38, 1307-1333, 2009.

[44] Zargar H, Ryan KL, Marshall JD. Feasibility study of a gap damper to control seismic isolator displacements in extreme earthquakes. Structural control and health monitoring, 20, 1159-1175, 2013.

[45]Yang H, Liu S, Yuan W. Experiment based seismic behavior investigation of a sliding controlled isolation system, Journal of Performance Constructed Facilities, 31(3), 1-13, 2017.

[46] Wang F, Yuan W, Dang X, Lin Z. Seismic Design of Nanchang Chao-yang Bridge, 94-100, 2014.

[47] Yuan W, Wang B, Cheung P, Cao X, Rong Z. Seismic performance of cable-sliding friction bearing system for isolated bridges. Earthquake Engineering and Engineering Vibration, 11, 173-183, 2012.

[48] Wei Z, Yuan W, Cheung P, Cao X, Rong Z. Seismic Performance of Continuous Girder Bridges Using Cable-sliding Friction Aseismic Bearing. Procedia Engineering, 14,914–921, 2011.

[49] Eatherton MR, Hajjar JF. Residual drifts of self-centering systems including effects of ambient building resistance. Earthquake Spectra, 27(3), 719-44, 2011.

[50] Ozbulut OE, Hurlebaus S. Optimal design of superelastic friction base isolators for seismic protection of highway bridges against near-field earthquakes. Earthquake Engineering and Structural Dynamic, 40(3), 273–291, 2011.

[51] Ozbulut OE, Hurlebaus S. A Comparative Study on the Seismic Performance of Superelastic-Friction Base Isolators against Near-Field Earthquakes, Earthquake Spectra, 28(3),1147–1163, 2012.

[52] Wang JQ, Shuai Li, Dezfuli FH, Alam MS. Sensitivity analysis and multi-criteria optimization of SMA cable restrainers for longitudinal seismic protection of isolated simply supported highway bridges, Engineering Structure, 189, 509–522, 2019.

[53] California Department of Transportation (CLATRANS). Seismic design criteria, Version 1.6, Sacramento, California; 2010.

[54] Mazzoni S, McKenna F, Scott M, Fenves G. Open system for earthquake engineering simulation (OpenSees). User command language manual. Berkeley: Pacific.

[55] Choi E, DesRoches R, Nielson B, Seismic fragility of typical bridges in moderate seismic zones," Engineering Structure, 26(2), 187-199, 2004.

[56] DesRoches R, Design of seismic cable hinge restrainers for bridges, Journal of Sound Vibration, 126(4), 500-509, 2000.

[57] PEER (Pacific Earthquake Engineering Research Center), University of California, Berkeley, CA, 2013.

[58] AASHTO guide specifications for LRFD seismic bridge design, Transportation Officials, no. May. 2011.

[59] Fang C, Zhong Q, Wang W, Hu S, and Qiu C, Peak and residual responses of steel moment-resisting and braced frames under pulse-like near-fault earthquakes, Engineering Structure, 177, 579-597, 2018.

Table 1 Test details for individual cables

Test code	Section construction	Diameter of monofilament wire(mm)	Length of free segment (mm)	Cross-sectional area (mm^2)	Loading pattern
7×7×1.2-C	7×7	1.2	164	55.39	Constant
7×7×1.2-I	7×7	1.2	164	55.39	Incremental
12×12×1.0-I	12×12	1.0	164	113.04	Incremental

Table 2 Parameters of theoretical model for SMA-cable-controlled bearing

Para-meter	h (mm)	l_{eff} (mm)	Friction coefficient (μ)	E (Gpa)	β_1	ε_{Ms}	ε_{Mf}	ε_{As}	ε_{Af}	σ_{Ms} (Mpa)	σ_{Mf} (Mpa)	σ_{As} (Mpa)	σ_{Af} (Mpa)
Value	220.0	229.4	0.005	16.5	0.19	0.03	0.1	0.075	0.003	495	714.5	302.1	49.5

Note: The parameters are explained in Section 3.1

Table 3 Parameters of numerical model

Bearing type	μ	l_{gap} (mm)	K_1 (kN/m)	l_{yield} (mm)	K_2 (kN/m)
Conventional	0.06	100	/	/	/
SMA-sliding	0.06	100	2.92×10^4	17.05	1.32×10^4
Steel-sliding	0.06	100	1.203×10^5	9.86	0

Table 4 Ground motions for system analysis

Earthquake No.	Record No.	Earthquake Name	Magnitude	Fault distance (km)	Vs30 (m/sec)	PGA (g)	PGV (m/s)
1	143	Tabas	7.35	2.05	766.77	0.86	1.23
2	879	Landers	7.28	2.19	1369.00	0.73	1.33
3	1106	Kobe	6.9	0.96	312.03	0.83	0.91
4	779	Loma Prieta	6.93	3.88	594.83	0.57	0.96
5	1197	Chi-Chi	7.62	3.12	542.61	0.76	0.85
6	1513	Chi-Chi	7.62	10.97	363.99	0.59	0.70
7	1549	Chi-Chi	7.62	1.83	511.18	1.01	0.66

Table 5 Response of peak displacement

Displacement (mm)					
No.	Conventional	SMA-sliding	IPF(%)	Steel-sliding	IPF(%)
1	326.60	152.60	53.28	132.20	59.52
2	278.70	136.20	51.13	119.90	56.98
3	245.10	123.50	49.61	114.40	53.33
4	255.80	153.40	40.03	141.60	44.64
5	171.40	119.50	30.28	110.60	35.47
6	337.60	132.60	60.72	122.10	63.83
7	172.30	108.90	36.80	104.60	39.29
Average	255.36	132.39	48.16	120.77	52.70

Table 6 Response of residual displacement

Residual displacement (mm)					
No.	Conventional	SMA-sliding	IPF(%)	Steel-sliding	IPF(%)
1	230.50	81.10	64.82	65.10	71.76
2	268.30	93.60	65.11	93.20	65.26
3	81.60	88.10	-7.97	77.50	5.02
4	98.53	10.50	89.34	7.20	92.69
5	54.30	51.80	4.60	6.90	87.29
6	297.30	57.70	80.59	65.90	77.83
7	81.30	16.70	79.46	38.50	52.64
Average	158.83	57.07	64.07	50.61	68.13

Table 7 Response of peak curvature ductility

Curvature ductility					
No.	Conventional	SMA-sliding	IPF(%)	Steel-sliding	IPF(%)
1	1.00	1.17	-17.58	1.22	-22.60
2	0.50	0.82	-64.46	0.80	-59.55
3	1.14	1.33	-16.67	1.61	-41.23
4	0.65	1.06	-63.58	1.24	-91.36
5	0.60	0.73	-22.03	1.04	-74.00
6	0.80	0.85	-6.60	1.08	-35.44
7	1.10	1.13	-2.73	1.12	-1.82
Average	0.83	1.01	-22.74	1.16	-40.32

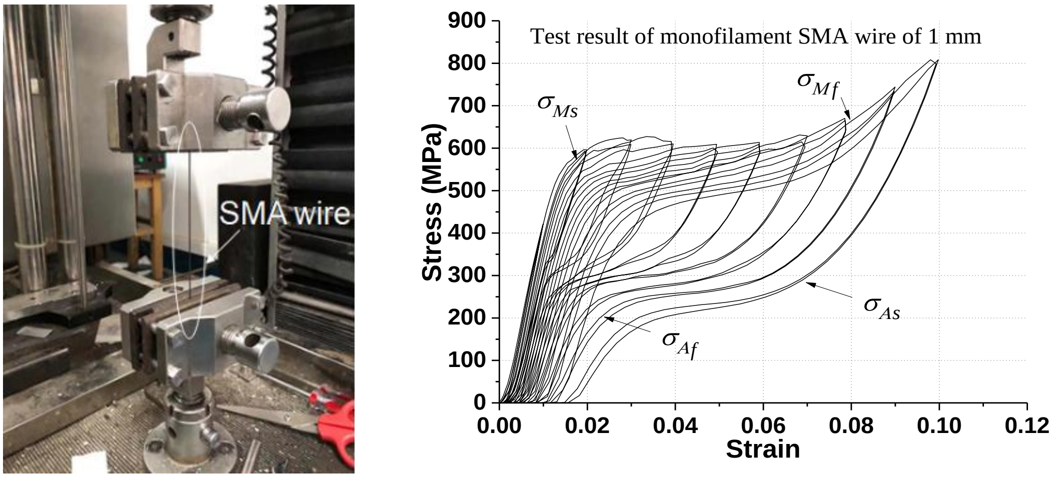

Fig. 1 SMA wire specimen and basic stress-strain responses of SMA wire with SE

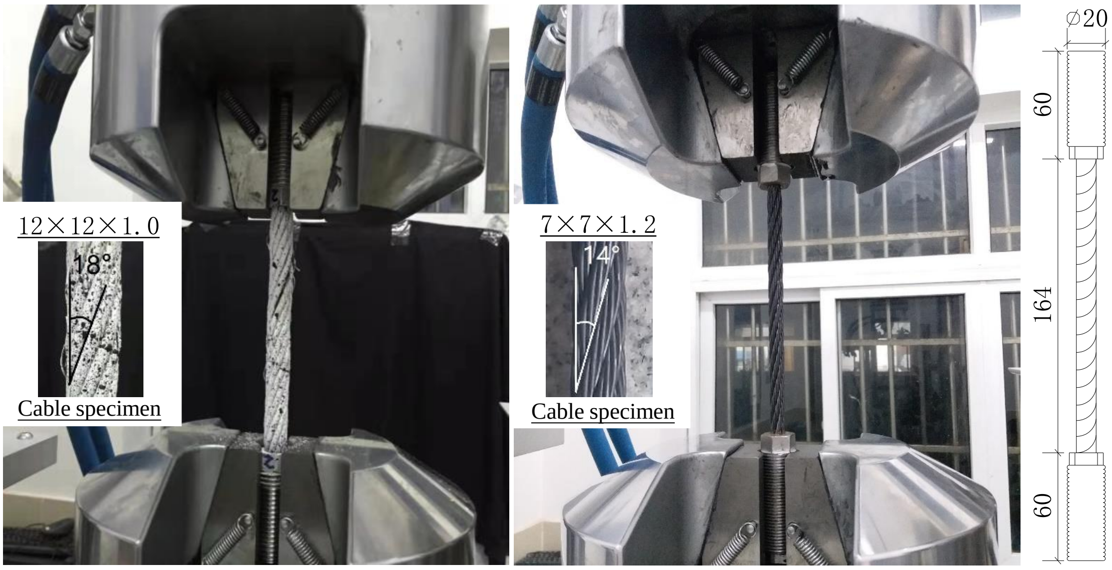

Fig. 2 SMA cable specimens and dimensions

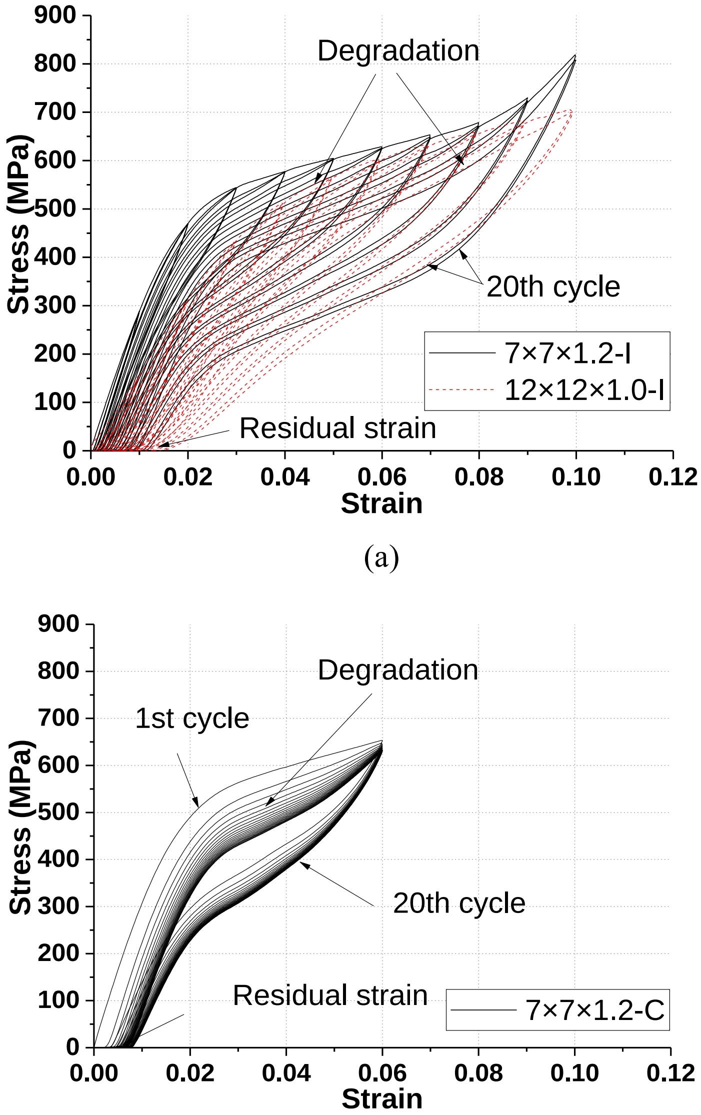

(a)

(b)

Fig. 3 Cyclic behavior of the SMA cable: a) incremental amplitudes, b) constant amplitude

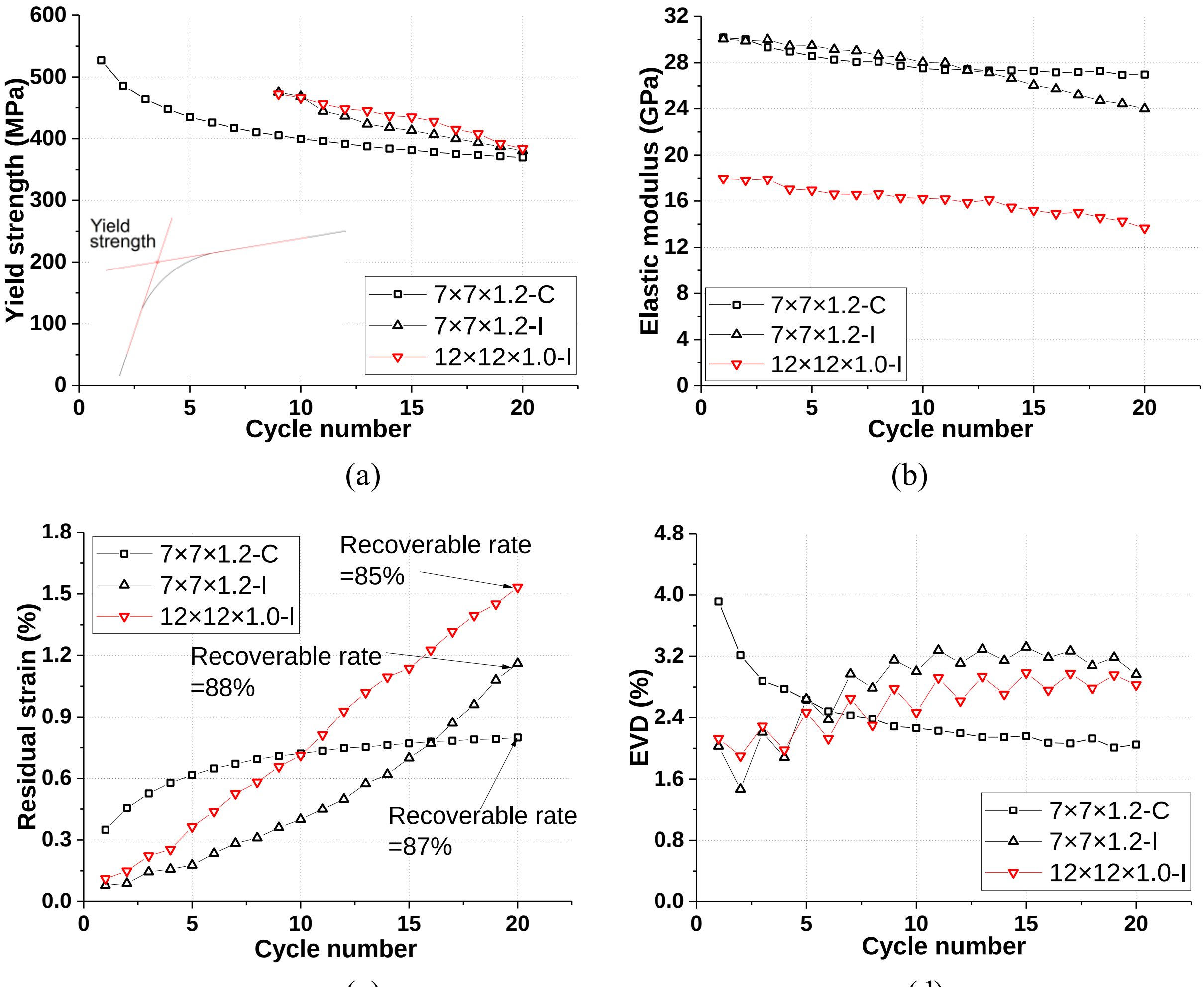

(a) (b)

(c) (d)

Fig. 4 Discussions of test results: a) yield strength, b) elastic modulus, c) residual strain, d) EVD

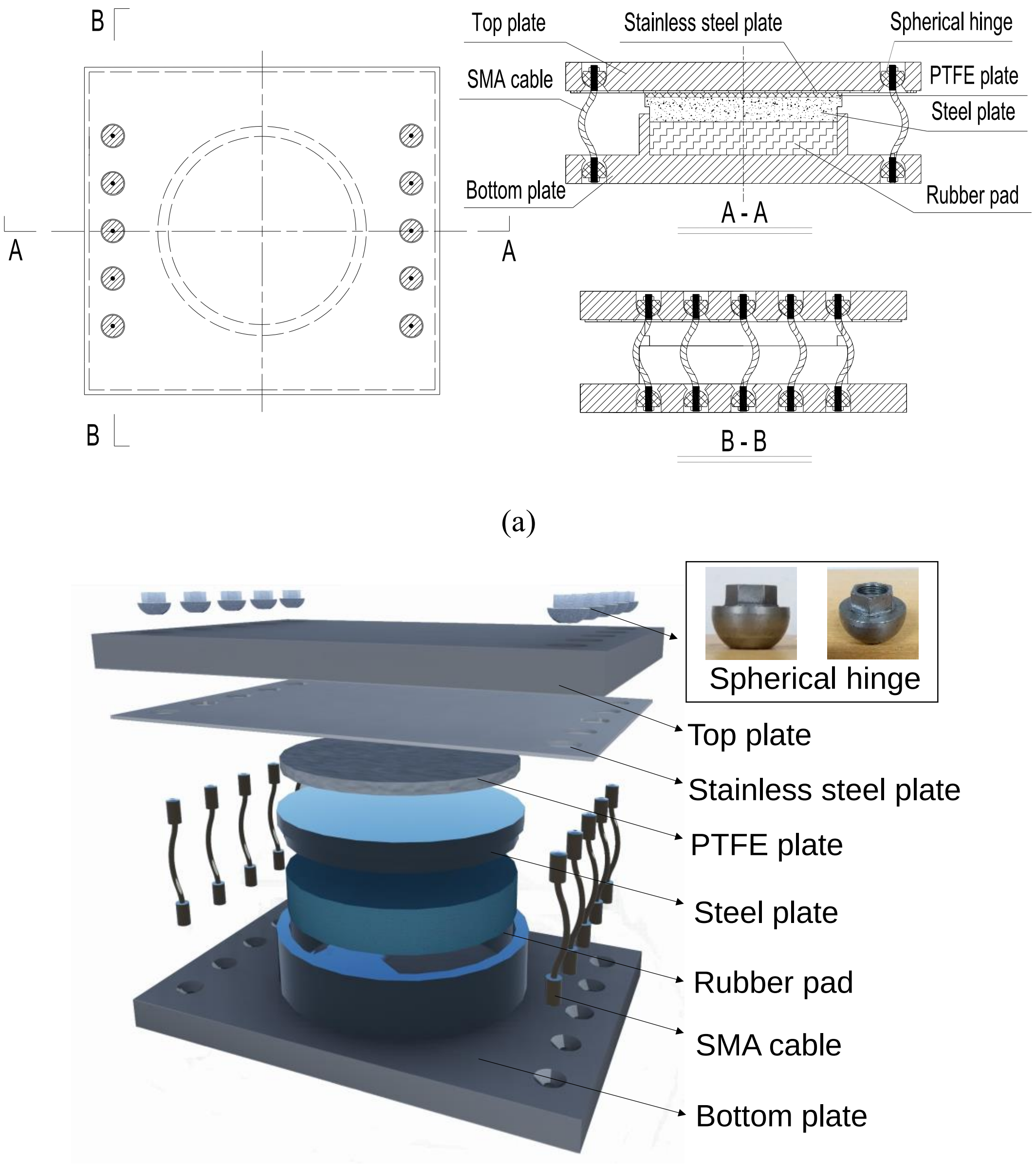

(a)

(b)

Fig. 5 Schematic illustration of SMA-sliding bearing: a) two-dimensional view, b) three-dimensional view

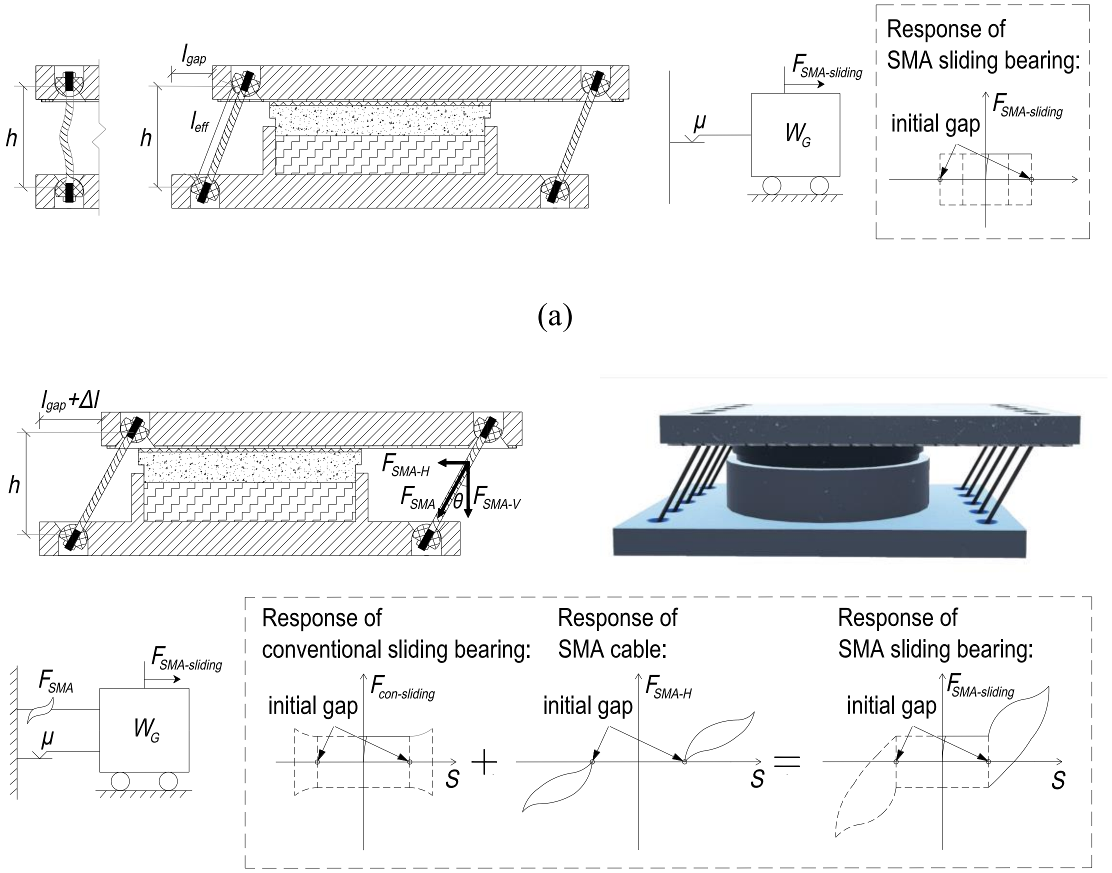

(a)

(b)

Fig. 6 Working principles of SMA-sliding bearing: a) before initial gap, b) after initial gap

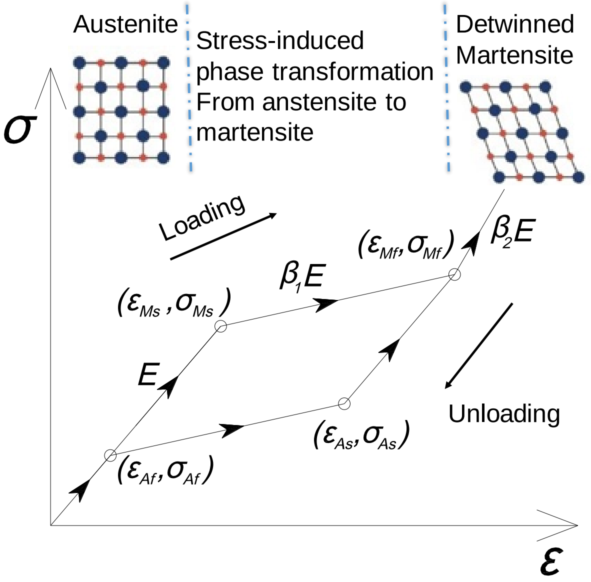

Fig. 7 Flag-shaped hysteresis model of SMA

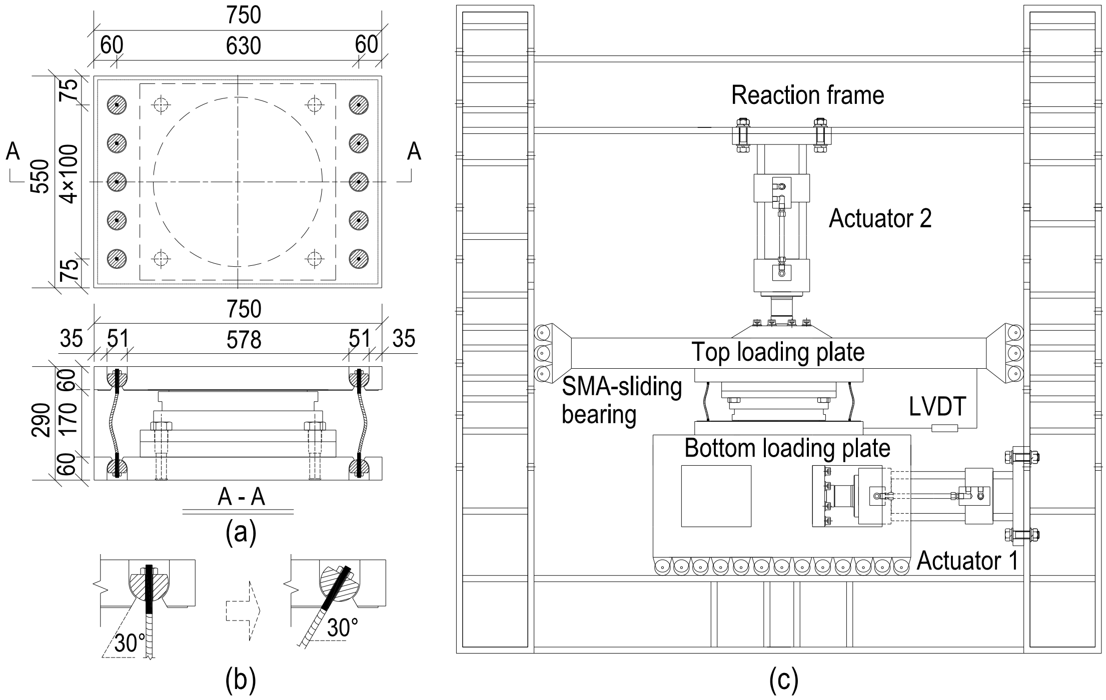

Fig. 8 Illustrations of a) geometric configuration and dimensions of specimens, b) detail of spherical hinge c) test setup

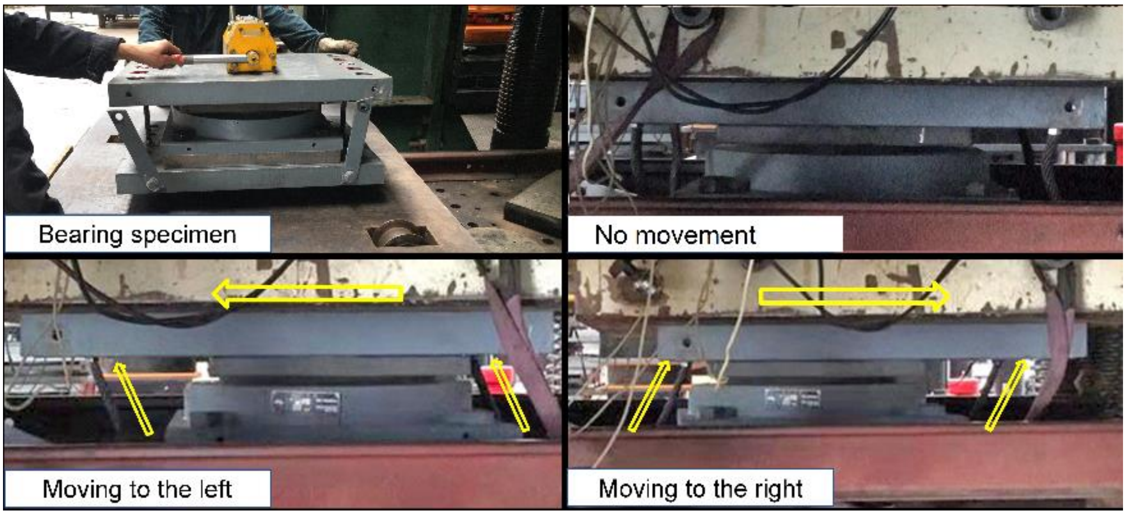

Fig. 9 Installation and deformation modes of SMA-sliding bearing

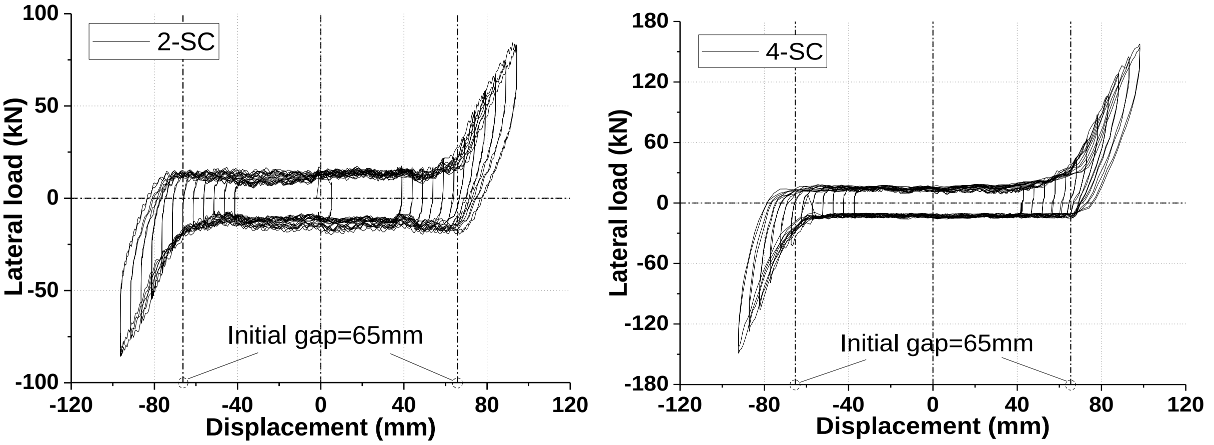

(a) (b)

Fig. 10 Load-displacement responses of specimens: a) 2-SC, b) 4-SC

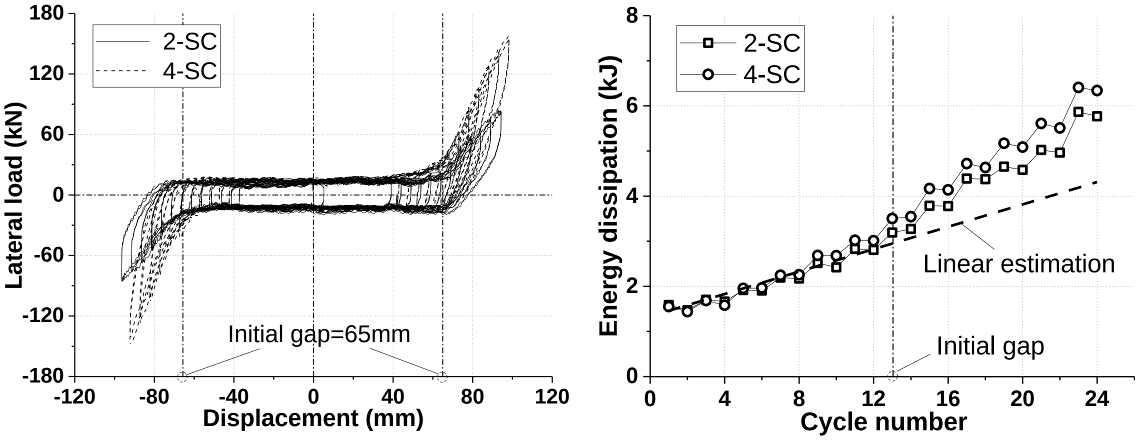

(a) (b)

Fig. 11 Comparison of test results: a) load-displacement response, b) energy dissipation

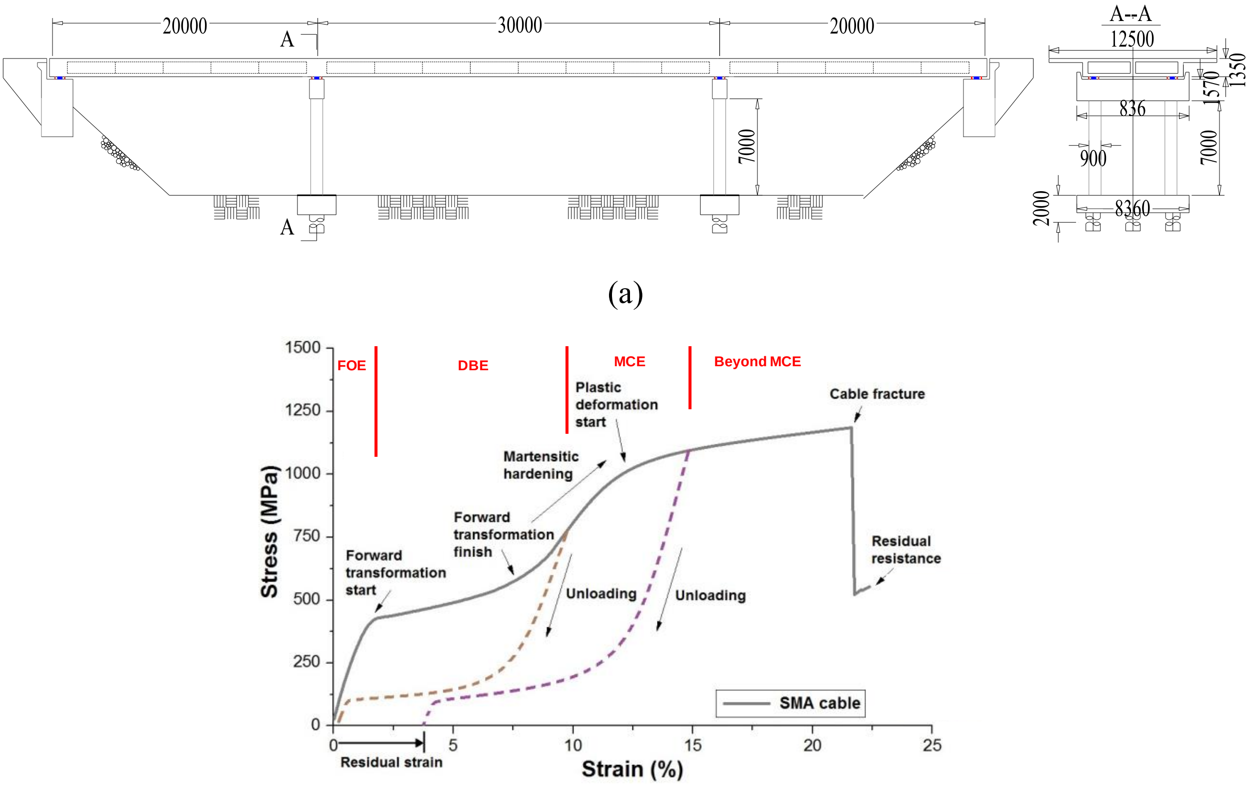

(a)

(b)

Fig. 12 a) Model of a three-span isolated continuous bridge (unit: mm), b) Diagram of design criteria

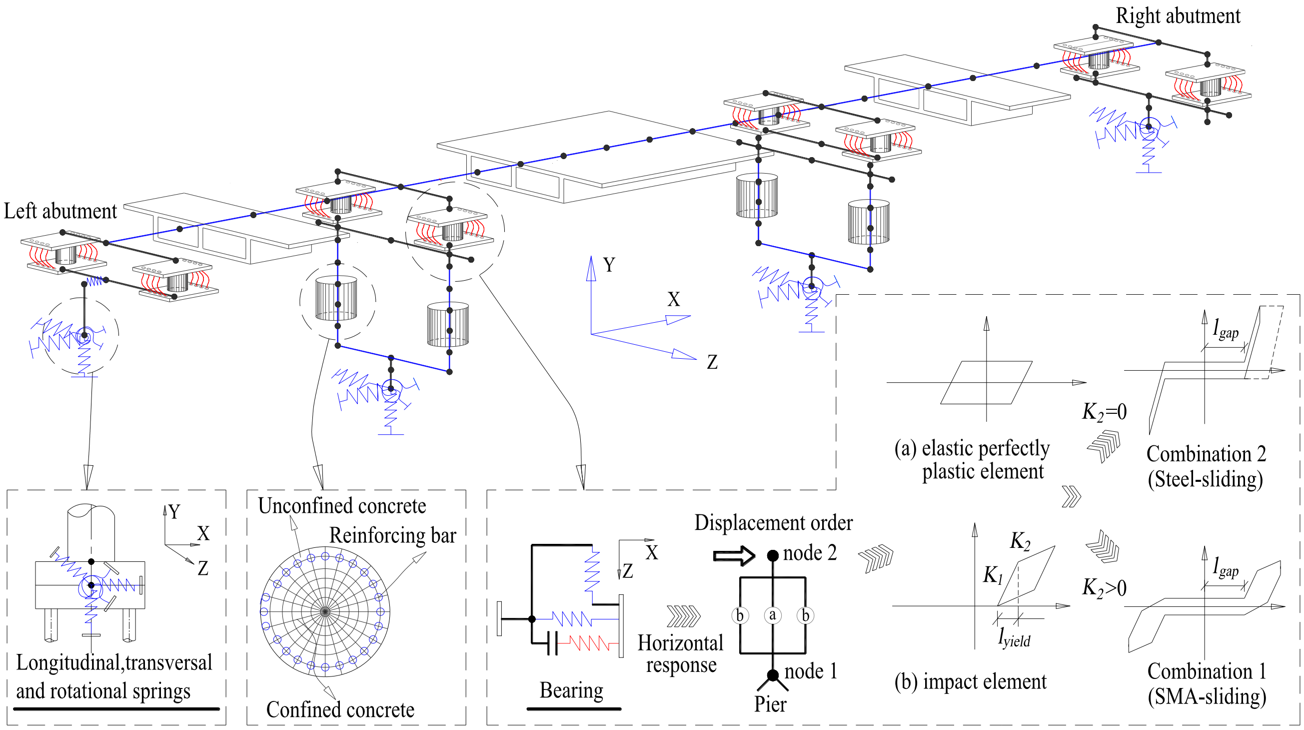

Fig. 13 Schematic illustration of FE bridge model and modeling details

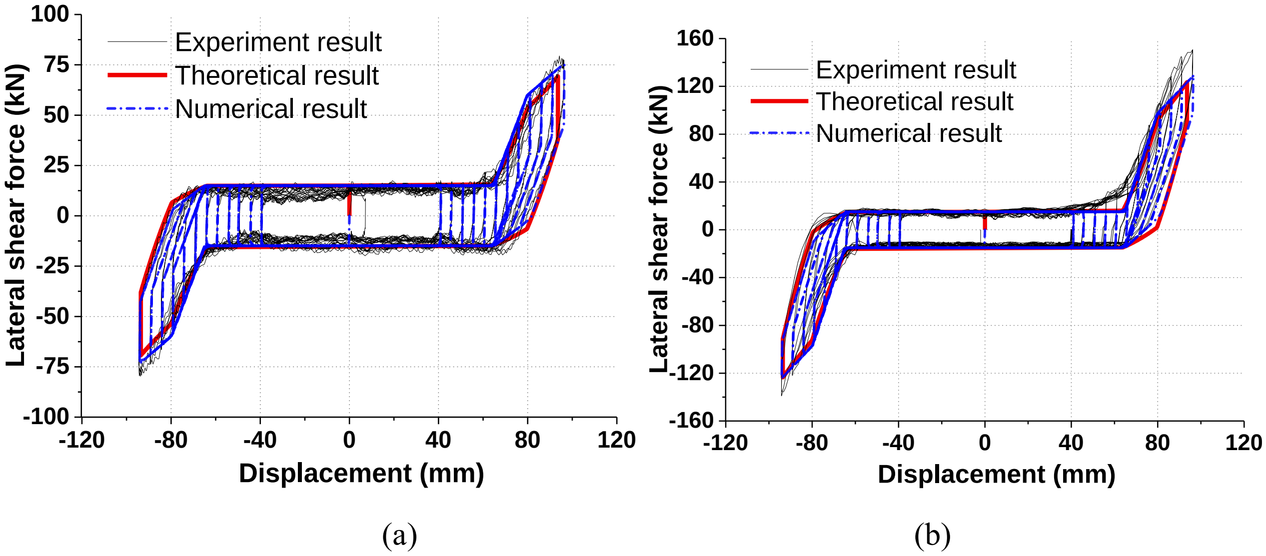

(a) (b)

Fig. 14 Validation of theoretical analysis result and numerical result: a) 2-SC, b) 4-SC

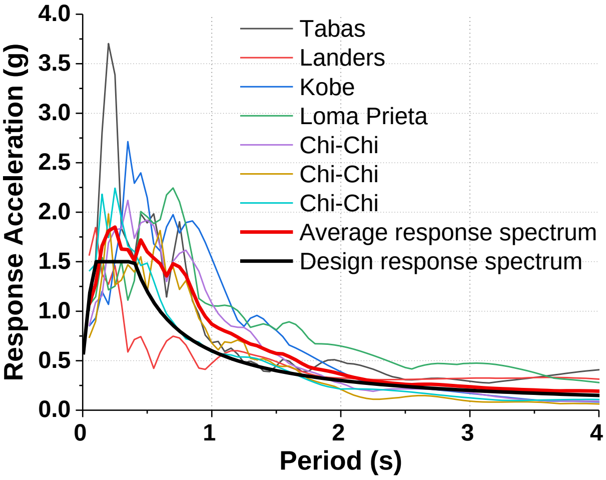

Fig. 15 Response spectra of selected ground motions

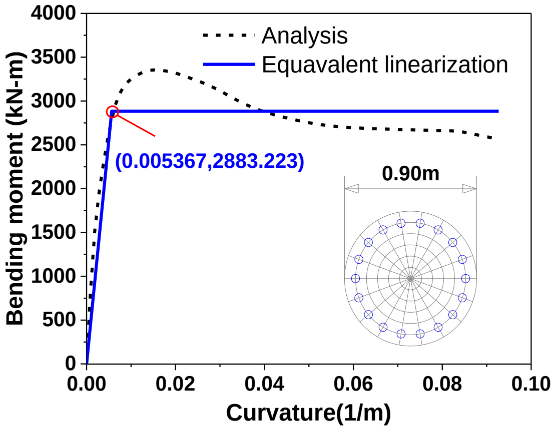

Fig. 16 Monotonic moment-curvature response of pier

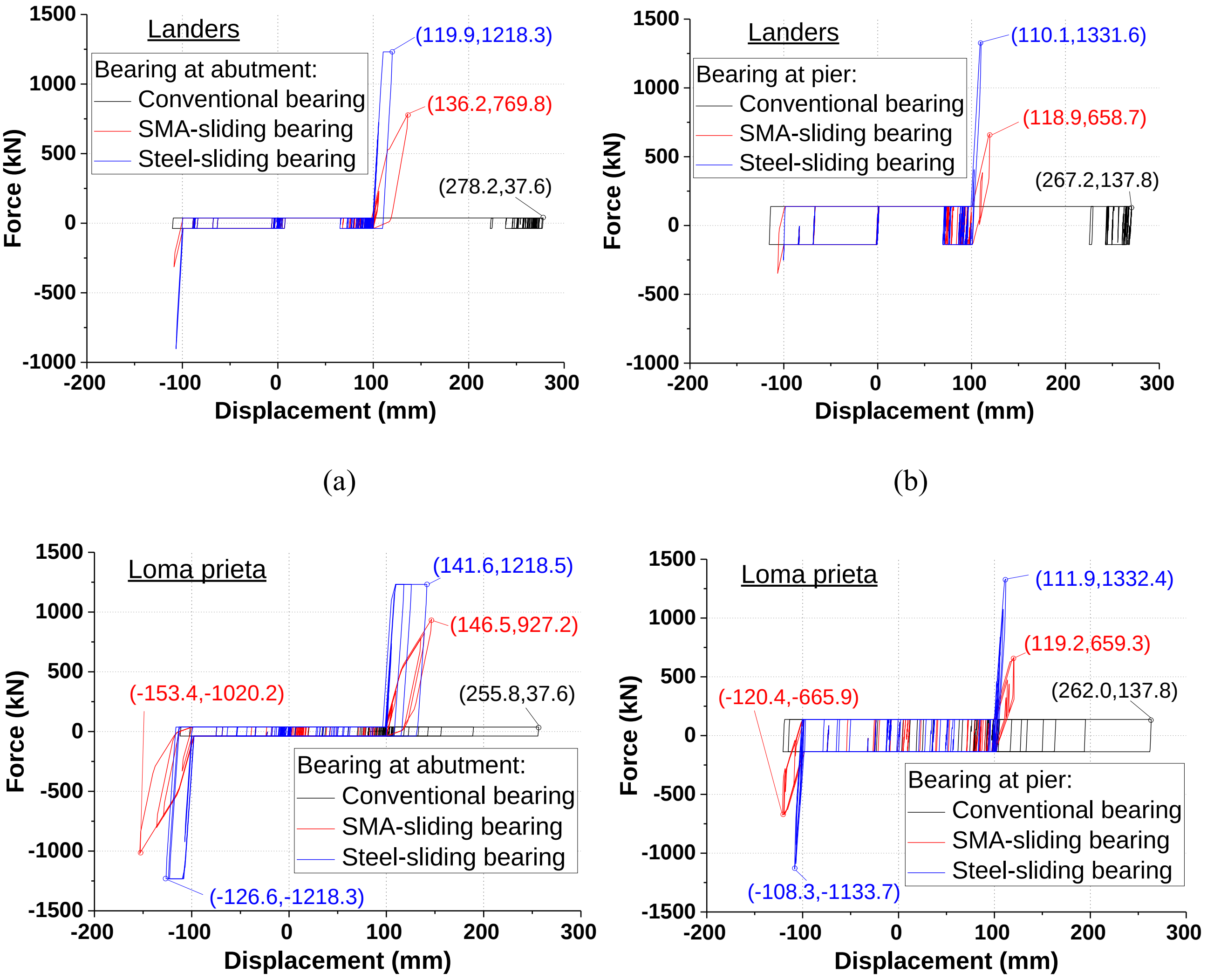

(a) (b)

(c) (d)

Fig. 17 Typical force-displacement response of conventional, SMA-sliding and Steel-sliding bearing

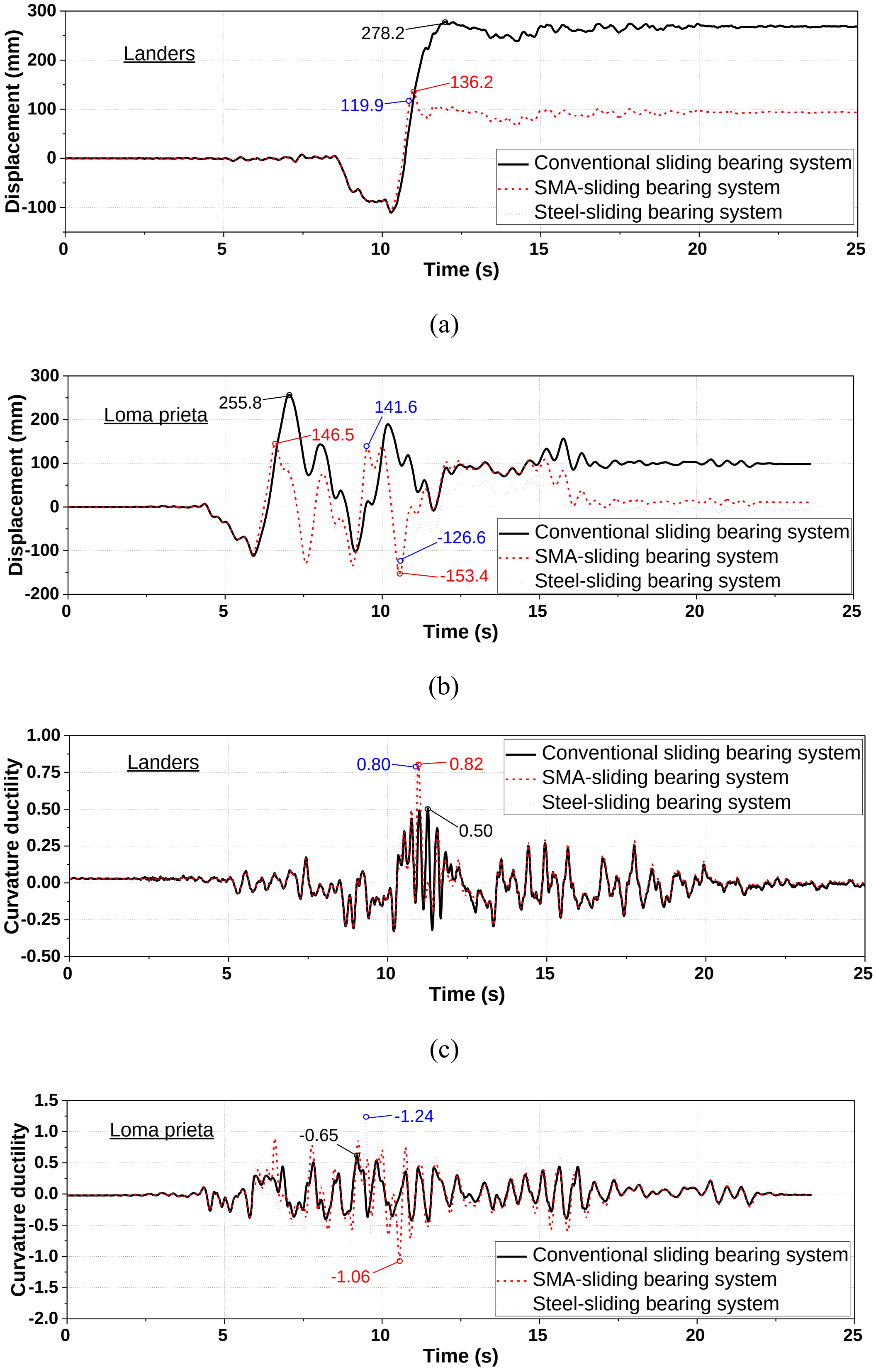

(a)

(b)

(c)

(d)

Fig. 18 Time history response of bearings displacement (at abutment) and pier curvature ductility